J. Electroanal. Chem., 323 (1992) 29–51
Elsevier Sequoia S.A., Lausanne
JEC 01801

Multidimensional integral equations: a new approach to solving microelectrode diffusion problems

Part 2. Applications to microband electrodes and the scanning electrochemical microscope

Michael V. Mirkin and Allen J. Bard
Department of Chemistry and Biochemistry, The University of Texas at Austin, Austin, TX 78712 (USA)

(Received 21 May 1991; in revised form 13 August 1991)

Abstract

The new approach to solving diffusion problems using multidimensional integral equations (equations containing multiple integrals) proposed in Part 1 is used to address microelectrode problems with two types of electrode geometry: two-dimensional linear diffusion and cylindrical diffusion in a thin-layer cell. The electrochemical current transients and cyclic voltammograms at a microband electrode as well as the response of a pair of parallel microbands working in the generator–collector mode are obtained. The current found with a scanning electrochemical microscope with either a conductive or an insulating substrate is also calculated using this approach. In both cases the current–potential curves can be computed for a simple electrode reaction with any value of heterogeneous rate constant and any shape of excitation signal. The theory for an electrode process with a successive first-order homogeneous chemical stage is also discussed.

INTRODUCTION

In Part 1 [1] we showed that many types of problems involving microelectrodes with non-uniformly accessible surfaces can be solved by use of multidimensional integral equations. The advantages of this approach are as follows: (1) high computational speed, especially in the case of electrode arrays and other systems with complicated geometry; (2) flexibility, allowing one to incorporate diverse excitation signals and different values of kinetic parameters without any significant changes in the program; (3) relative simplicity of the algorithms; (4) uniform description of various types of microelectrodes. In Part 1 [1] the numerical treatment of a microdisk was shown. We now consider two other, substantially

different, cases: microband electrodes (or paired parallel bands) and the scanning electrochemical microscope (SECM).

Microband electrodes, which have extremely small widths, have been the subject of many experimental studies [2–6]. However, the theoretical description of such electrodes is less well developed. Unlike a microdisk, no true steady state can be achieved with a microband electrode. Therefore no theoretical expression for the steady-state current (such as those for the microdisk or the microsphere) is available. Non-steady-state calculations appear to be complicated. Even in the simplest case of chronoamperometry at a microband with a pure diffusion control, no single analytical approximation for the whole time domain has been obtained so far. Aoki et al. [7], using extremely heavy mathematics, derived an integral expression describing the long-time region. They also obtained two rather complicated analytical approximations for short and long times which cannot be combined into a single smooth curve. Two other approximations proposed by Szabo et al. [8] appear simpler; however, their long-time approximation is the result of an arbitrary fit and is not physically intuitive. The exact results for diffusion-controlled chronoamperometry at a microband were obtained by solution of an integral equation in Laplace transform space with successive numerical inversion [9].

Deakin et al. [10] performed a digital simulation of quasi-reversible cyclic voltammograms at a microband electrode, and reported a good fit to the experimental curves for ferrocene oxidation. With this general formulation of the diffusion problem, this approach should be useful in the computation of voltammograms for electrode processes of any degree of reversibility, as well as for chronoamperograms etc. Surprisingly, Deakin et al. presented results only for totally reversible reactions with the whole set of kinetic and experimental parameters allowing quantitative comparison. The main conclusion of ref. 10, as well as in its continuation [11], is the existence of the analogy between a band and a hemicylindrical electrode. However, this analogy is less useful for quantitative interpretations because the equivalency is not straightforward, and the solutions for a cylindrical electrode itself are not very simple.

The microband theory we present below can easily be extended to an array of parallel bands, particularly to the double-band electrode. This type of microelectrode array has been used in homogeneous kinetic studies [12,13] as well as in flow injection analysis and liquid chromatography [14] and for the determination of diffusion coefficients [15]. Substantial computer power was required for the time-independent simulation of this problem [12,13].

Simulation of the SECM is quite challenging. Several different techniques have been employed for this system. Kwak and Bard [16] used a finite-element method with an exponentially expanding grid to simulate the steady-state current with both conductive and insulating substrates. A Krylov algorithm was applied to compute diffusion-controlled transients [17]. Recently the theory of SECM in both the steady-state and chronoamperometric feedback modes was developed for the E_rC_i mechanism using the ADI finite-difference method [18]. We report here a semi-

analytical solution of the problem taking into account quasi-reversible charge transfer, finite size of the substrate and variable potentials of both tip and substrate.

In the next section we deal with details of the mathematical treatment and the approach used in obtaining numerical results. The results of the computations for microbands and the SECM are contained in the third section, which may be consulted directly by readers less interested in the mathematical details.

THEORY AND ALGORITHMS

Microband electrode

We have recently shown [1] that the two-dimensional integral equation

$$\frac{f(t, x)\ \exp\{\alpha fn[E(t) - E^\circ]\}/\Lambda + 1}{1 + \exp(fn[E(t) - E^\circ])} = -\frac{1}{2\pi}\int_A du \int_0^t \frac{\exp\left[-(x-u)^2/4(t-\tau)\right]}{t-\tau} f(\tau, u)\ d\tau \tag{1}$$

describes the electrochemical behavior of an inlaid microband electrode (or an array of parallel microbands) for the case of equal diffusion coefficients. The total dimensionless faradaic current is calculated according to

$$I(t) = -\int_A f(t, x)\ dx \tag{2}$$

where the local dimensionless flux is $f(t, x) = -(w/2Dc^\circ)f(T, X)$ and the total dimensionless faradaic current is $I(t) = I(T)/nFc^\circ DL$; for other dimensionless variables, see ref. 1. In the case of a single microband (Fig. 1(a)), the conductive surface area A is represented by the interval $(-1, 1)$. A set of such intervals corresponds to an array of bands (Fig. 1(b)).

Equation (1) can be solved with the same algorithm as that proposed for a microdisk in ref. 1. The only difference is that the kernel in integral (1) is much simpler. As described in ref. 1, one can obtain from eqn. (1) for each time t_k a system of m linear equations

$$\mathbf{A}\boldsymbol{f} = \boldsymbol{b} \tag{3}$$

where the components of the vectors $\boldsymbol{f}$ and $\boldsymbol{b}$ are

$$f_l = f(t_k, x_l) \tag{4}$$

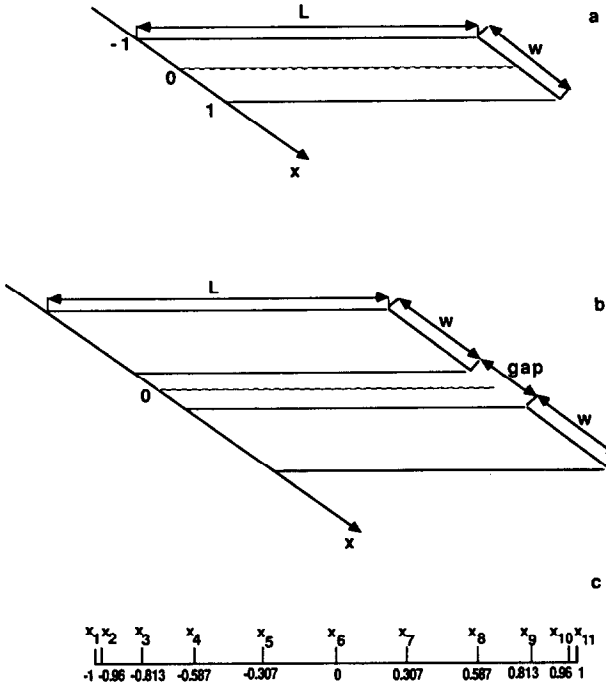

Fig. 1. Scheme of (a) an inlaid band electrode, (b) a double-band electrode and (c) a non-uniform spatial grid over the band surface. The points x_i at which the local flux is to be computed are indicated.

and

$$b_l = -\frac{2\pi}{1+\exp\{fn[E(t_k)-E^\circ]\}} - \sum_{j=1}^{m} F(x_l, x_j, t_{k-1})\Delta x_j \tag{5}$$

$$F(x_l, x_j, t_{k-1}) = \sum_{i=1}^{k-1} \frac{\exp\left[-(x_l-x_j)^2/4(t_k-t_i)\right]}{t_k-t_i} f(t_i, x_j)\Delta t_i + \frac{f(t_{k-1}, x_j)}{2}\int_{t_{k-1}}^{t_k} \frac{\exp\left[-(x_l-x_j)^2/4(t_k-\tau)\right]}{t_k-\tau}\,d\tau \tag{6}$$

As in ref. 1, $\Delta t_i = (t_{i+1} - t_{i-1})/2$ for $1 < i < k-1$, $\Delta t_1 = t_2/2$, and $\Delta t_{k-1} = (t_{k-1} - t_{k-2})/2$; each point x_j (excluding the two points x_1 and x_m) is located in the middle of the interval (a_{j-1}, a_j), and $\Delta x_j = a_j - a_{j-1}$. The elements of the matrix **A** are

$$a_{lj}|_{l\neq j} = \tfrac{1}{2}\int_{a_{j-1}}^{a_j} du \int_{t_{k-1}}^{t_k} \frac{\exp\left[-(x_l-u)^2/4(t_k-\tau)\right]}{t_k-\tau}\,d\tau = \tfrac{1}{2}(a_j - a_{j-1})\int_{t_{k-1}}^{t_k} \frac{\exp\left[-(x_l-x_j)^2/4(t_k-\tau)\right]}{t_k-\tau}\,d\tau \tag{7}$$

and

$$a_{ll} = \frac{2\pi \exp\{\alpha fn[E(t_k) - E^\circ]\}}{\Lambda(1 + \exp\{fn[E(t_k) - E^\circ]\})} + \tfrac{1}{2}\int_{a_{j-1}}^{a_j} du \int_{t_{k-1}}^{t_k} \frac{\exp\left[-(x_l - u)^2/4(t_k - \tau)\right]}{t_k - \tau} d\tau \tag{8}$$

It should be noted that $a_{lj} = a_{jl}$.

By solving the system of eqn. (3) for each step of integration, one can calculate m values of the diffusion flux $f(t_k, r_j)$ and compute the total current according to eqn. (2). Unlike the similar equations derived in ref. 1 for a microdisk, analytical expressions are available for the integrals (6)–(8). Using these expressions one can remove all integration subroutines and significantly simplify the computer program used to obtain numerical results. However, this modification does not result in any gain in CPU time, and therefore it will be not considered further in this paper.

The procedure for solving eqn. (1) for two (or more) microbands is essentially the same. The only difference is the necessity of substituting in eqns. (5) and (8) different values of the parameters (E, Λ etc.) corresponding to different bands. The computations have shown that a 42-point space grid (equivalent to the 21-point grid used for single-band modeling) produces instabilities. This is consistent with the appearance of instabilities as a result of increasing the number of spatial points, as reported in ref. 19 where one-dimensional integral equations were used for modeling a microdisk. An 11-point grid (over each band surface) (Fig. 1(c)) appeared to be much more stable. This grid is generated by the following formulae: $x_1 = -1$; $i = 1, 10, x_{i+1} = x_i + (1/75)(-7 + 11i - i^2)$; $a_1 = -1$, $a_{11} = 1$, $a_{i+1} + a_i = 2x_i$ for all other i. This grid is also recommended for single-band computations.

Scanning electrochemical microscopy

SECM [20] involves a microelectrode (tip), usually a disk embedded in an insulating sheath, in close proximity to a substrate. The effect of the substrate, either an insulator or a conductor, on the tip current can be used in the characterization or imaging of the substrates, in their modification [21], and for studying kinetics of heterogeneous reactions on the substrate or homogeneous reactions that take place in the gap between tip and substrate [18,22]. These different applications require substantially different mathematical descriptions. The process of imaging is usually performed under quasi-steady-state conditions. A theory for the steady-state current [16] is much simpler than the non-steady-state mathematics required for transient and kinetic experiments. The model used in the present work describes an SECM experiment under the conditions of a small substrate and an inlaid tip. With a small substrate, one can use all the advantages of microelectrodes (in particular, both electrodes can work in a steady-state regime) as well as significantly improve the accuracy of measuring the relatively small current owing to the flux from the tip. The estimation of the effect of

substrate size is also useful in imaging considerations for highly irregular surfaces composed of different materials [23]. The assumption of an inlaid tip simplifies the theory significantly and allows one to remove some of the geometrical uncertainties (see the next section).

The solution of the SECM diffusion problem obtained in ref. 1 is as follows (the change of sign in the expression for f_s should be noted):

$$\frac{f_t(t, r)\ \exp\{\alpha_t f_t n[E_t(t) - E^\circ]\}/\Lambda_t + 1}{1 + \exp\{f_t n[E_t(t) - E^\circ]\}}$$

$$= -\frac{1}{2\gamma}\int_0^H u\ \mathrm{d}u \int_0^t \frac{\exp[-(r^2+u^2)/4(t-\tau)]}{t-\tau}$$

$$\times I_0\left[\frac{ru}{2(t-\tau)}\right]\left\{f_s(\tau, u)\theta_4\left[0\middle|\frac{i\pi(t-\tau)}{\gamma^2}\right] + f_t(\tau, u)\theta_3\left[0\middle|\frac{i\pi(t-\tau)}{\gamma^2}\right]\right\}\mathrm{d}\tau \tag{9}$$

$$\frac{f_s(t, r)\ \exp\{\alpha_s f_s n[E_s(t) - E^\circ]\}/\Lambda_s + 1}{1 + \exp\{f_s n[E_s(t) - E^\circ]\}}$$

$$= -\frac{1}{2\gamma}\int_0^H u\ \mathrm{d}u \int_0^t \frac{\exp[-(r^2+u^2)/4(t-\tau)]}{t-\tau}$$

$$\times I_0\left[\frac{ru}{2(t-\tau)}\right]\left\{f_s(\tau, u)\theta_3\left[0\middle|\frac{i\pi(t-\tau)}{\gamma^2}\right] + f_t(\tau, u)\theta_4\left[0\middle|\frac{i\pi(t-\tau)}{\gamma^2}\right]\right\}\mathrm{d}\tau \tag{10}$$

where

$$f_t(t, r) = \left[\frac{\partial c(t, r, z)}{\partial z}\right]_{z=0}$$

$$f_s(t, r) - \left[\frac{\partial c(t, r, z)}{\partial z}\right]_{z=\gamma}$$

$$I_t(t) = -\frac{\pi}{2}\int_0^1 f_t(t, r) r\ \mathrm{d}r = \frac{I_t(T)}{4n_t Fc^\circ DR_t}$$

$$I_s(t) - \frac{\pi}{2}\int_0^h f_s(t, r) r\ \mathrm{d}r = \frac{I_s(T)}{4n_s Fc^\circ DR_t}$$

and $H = \max(h, 1)$. The numerical solution of eqns. (9) and (10) is essentially analogous to that described above for a microband or for a microdisk [1]. The algorithm becomes simpler with an assumption of equal tip and substrate radii ($h = 1$), which allows one to use the same spatial grid for both electrodes. As

described in ref. 1, each integration step requires solution of the system of linear equations (3). Let $m = 2m1$ be the total number of r-points over the tip and substrate surfaces. In all computations described here $m1 = 6$. Then the following equations determine the elements of the matrix **A** and the components of the vectors f and b at $t = t_k$:

$$a_{lj}\,|_{\,l\neq j,\,|l-j|\neq m1}$$

$$= \frac{r_j \Delta r_j}{2\gamma} \int_{t_{k-1}}^{t_k} \frac{\exp\left[-\left(r_l^2 + r_j^2\right)/4(t-\tau)\right]}{t-\tau} I_0\left[\frac{r_l r_j}{2(t-\tau)}\right] \theta_i\left[0\left|\frac{i\pi(t-\tau)}{\gamma^2}\right.\right] \mathrm{d}\tau$$

if $l \leq m1$ and $j \leq m1$ or $m1 \leq l$ and $m1 \leq j$, $i = 3$; else $i = 4$; $\Delta r_j = a_j - a_{j-1}$ (11)

$$a_{ll} = \frac{1}{2\gamma} \int_{a_{j-1}}^{a_j} u\,\mathrm{d}u \int_{t_{k-1}}^{t_k} \frac{\exp\left[-\left(r_l^2 + u^2\right)/4(t-\tau)\right]}{t-\tau}$$

$$\times I_0\left[\frac{ru}{2(t-\tau)}\right] \theta_3\left[0\left|\frac{i\pi(t-\tau)}{\gamma^2}\right.\right] \mathrm{d}\tau + \frac{2\exp\{\alpha_i f_i n[E_i(t) - E^\circ]\}}{\Lambda_i(1 + \exp\{f_i n[E_i(t) - E^\circ]\})}$$

if $l \leq m1$, $i = \mathrm{t}$; if $m1 < I$, $i = \mathrm{s}$ (12)

$$a_{lj}\,|_{\,|l-j|=m1} = \frac{1}{2\gamma} \int_{a_{j-1}}^{a_j} u\,\mathrm{d}u \int_{t_{k-1}}^{t_k} \frac{\exp\left[-\left(r_l^2 + u^2\right)/4(t-\tau)\right]}{t-\tau}$$

$$\times I_0\left[\frac{r_l u}{2(t-\tau)}\right] \theta_4\left[0\left|\frac{i\pi(t-\tau)}{\gamma^2}\right.\right] \mathrm{d}\tau \tag{13}$$

$f_l = f_i(t_k, r_l)$; if $l \leq m1$, $i = t$; if $m1 < l$, $i = \mathrm{s}$ (14)

$$b_l = -\frac{2}{1 + \exp\{f_i n[E_i(t) - E^\circ]\}} - \sum_{j=1}^{m} F(r_l, r_j, t_{k-1});$$

if $l \leq m1$, $i = t$; if $m1 < l$, $i = \mathrm{s}$ (15)

$$F(r_l, r_j, t_{k-1}) = \frac{r_j \Delta r_j}{2\gamma} \sum_{n=1}^{k-1} \frac{\exp\left[-\left(r_j^2 + r_l^2\right)/4(t_k - t_n)\right]}{t_k - t_n}$$

$$\times I_0\left[\frac{r_j r_l}{2(t_k - t_n)}\right] f(t_n, r_j) \theta_i\left[0\left|\frac{i\pi(t_k - t_n)}{\gamma^2}\right.\right] \Delta t_n + a_{lj} f(t_{k-1}, r_j)$$

$l \neq j$, $|I - j| \neq m1$; if $l \leq m1$ and $j \leq m1$ or $m1 \leq l$ and $m1 \leq j$, $i = 3$; else $i = 4$ (16)

$$F(r_l, r_j, t_{k-1})$$

$$= \frac{r_j \Delta r_j}{2\gamma} \sum_{n=1}^{k-1} \frac{\exp[-r_l^2/2(t_k - t_n)]}{t_k - t_n} I_0\left[\frac{r_l^2}{(t_k - t_n)}\right] f(t_n, r_l)\theta_i\left[0\middle|\frac{i\pi(t_k - t_n)}{\gamma^2}\right]\Delta t_n$$

$$+ \frac{f(t_{k-1}, r_l)}{2\gamma} \int_{a_{j-1}}^{a_j} u\, du \int_{t_{k-1}}^{t_k} \frac{\exp[-(r_l^2 + u^2)/4(t-\tau)]}{t-\tau}$$

$$\times I_0\left[\frac{ru}{2(t-\tau)}\right]\theta_i\left[0\middle|\frac{i\pi(t-\tau)}{\gamma^2}\right] d\tau$$

if $l = j$, $i = 3$; if $|l - j| = m1$, $i = 4$ (17)

Taking into account the equality of the integrals in a_{lj} and a_{jl}, one can reduce the amount of computation. The θ functions in eqns. (11)–(17) can be computed according to [24]

$$\theta_3\left(0\middle|\frac{i\pi t}{\gamma^2}\right) = \frac{\gamma}{(\pi t)^{1/2}}\left[1 + 2\sum_{n=1}^{\infty} \exp\left(-\frac{n^2\gamma^2}{t}\right)\right] \tag{18}$$

$$\theta_4\left(0\middle|\frac{i\pi t}{\gamma^2}\right) = \frac{2\gamma}{(\pi t)^{1/2}} \sum_{n=1}^{\infty} \exp\left[-\frac{(n-0.5)^2\gamma^2}{t}\right] \tag{19}$$

The number of terms in the series satisfies the inequality $(n^2\gamma^2/t) \leq 20$ for the largest n value.

In the case of an infinite insulating substrate ($f_s(t, r) = 0$) one need only solve eqn. (9) without the term containing f_s. In this case the algorithm is identical to that described in ref. 1 (eqns. 82–89) with the additional multiplier $\theta_3[0 \mid i\pi(t - \tau)/\gamma^2]$.

In this section we have presented only basic ideas for solving eqns. (1), (9) and (10). A number of practical details allowing one to save computer time and to improve the stability of the solution will be discussed elsewhere. Standard subroutines used to solve the linear system (eqn. (3)), to evaluate the values of the single and double integrals and to compute the Bessel function $I_0(x)$ have been listed previously [1].

RESULTS AND DISCUSSION

Single-microband electrodes

The computation of the I–E curves for a microband electrode was essentially the same as that described previously [1] for a disk electrode, and the microdisk program was easily changed for the present computations. This illustrates the flexibility of this approach. The microband computations were even faster than those performed in ref. 1; computation of each I–t transient (Fig. 2) required

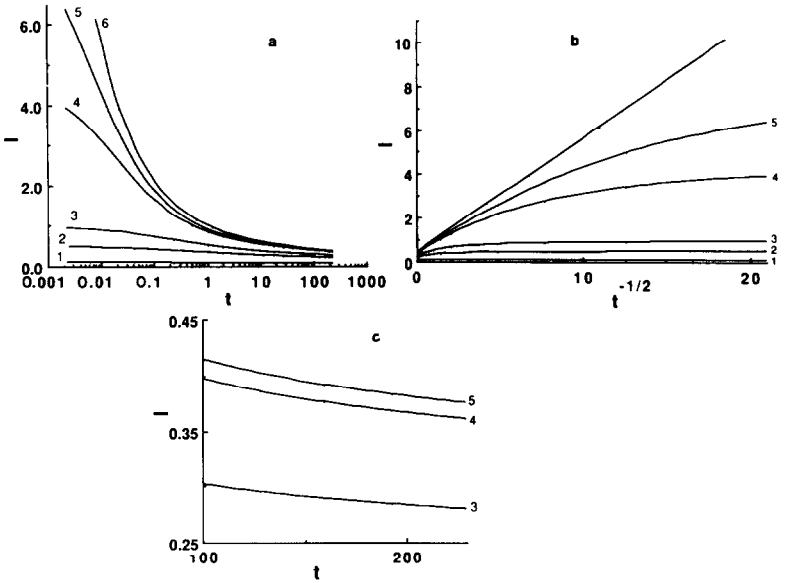

Fig. 2. Dimensionless chronoamperometric current at a microband electrode as a function of (a) t and (b) $t^{-1/2}$; (c) long-time part of the transients. $E = E°$; $\Lambda = wk_s/2D$; $t = 4DT/w^2$; $I(t) = I(T)/nFc°DL$. Curve 1, $\Lambda = 0.05$; curve 2, $\Lambda = 0.25$; curve 3, $\Lambda = 0.5$; curve 4, $\Lambda = 2.5$; curve 5, $\Lambda = 5.0$; curve 6, $\Lambda = 50$.

about 1 s of the CRAY Y-MP8/864 CPU time (with an established r- and t- grid). Computing a CV with more than 100 time points required about 5 s using a 21-point space grid constructed by means of the symmetrical continuation of the grid shown in Fig. 5 of ref. 1 on the interval $(-1, 0)$. With the 11-point grid described above, the computations were twice as fast without any loss in accuracy.

There was very good agreement between our results and those of Coen et al. [9] for an I–t transient for an essentially diffusion-controlled process (Fig. 3). The minor discrepancies that arise in the short-time region are owing to the kinetic limitations. When the applied potential is not far from $E_{1/2}$, one can see the influence of the charge transfer rate on the shape of the chronoamperograms (Fig. 2). These dimensionless curves computed for a potential $E = E°$ are functions of the kinetic parameter Λ. $\Lambda = 50$ (curve 6) corresponds to the process which is almost Nernstian in the chosen time region. $\Lambda \leq 0.05$ (curve 1) corresponds to a totally irreversible process. The transients shown in Fig. 2 allow one to estimate the magnitude of the heterogeneous rate constant k_s. This may be quite useful for large k_s with very small band electrodes [2,3]. For example, with a microband of width 50 nm one can easily distinguish curves 3, 4 and 5 (Fig. 2(c)) corresponding to values of k_s of 2 cm/s, 10 cm/s and 20 cm/s respectively.

Cyclic voltammograms (CVs) for microband electrodes and different values of the kinetic parameters and scan rate (Figs 4 and 5) were computed from eqns. (1)

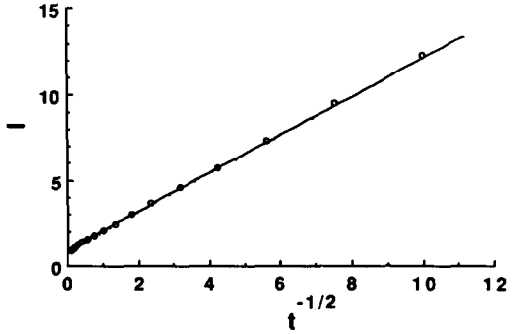

Fig. 3. Dimensionless transient at a microband electrode computed from eqn. (1): $\Lambda = 5$, $\alpha = 0.5$, $fn(E - E^\circ) = -5.87$. Circles are for a diffusion-controlled process [9]. (I and t defined in Fig. 2.)

and (2). One can see from eqn. (1) that the shape of the dimensionless CV is a function of Λ, α and the dimensionless potential $fn[E(t) - E^\circ]$. If the initial potential and the reversal point are chosen sufficiently far from the peak potential,

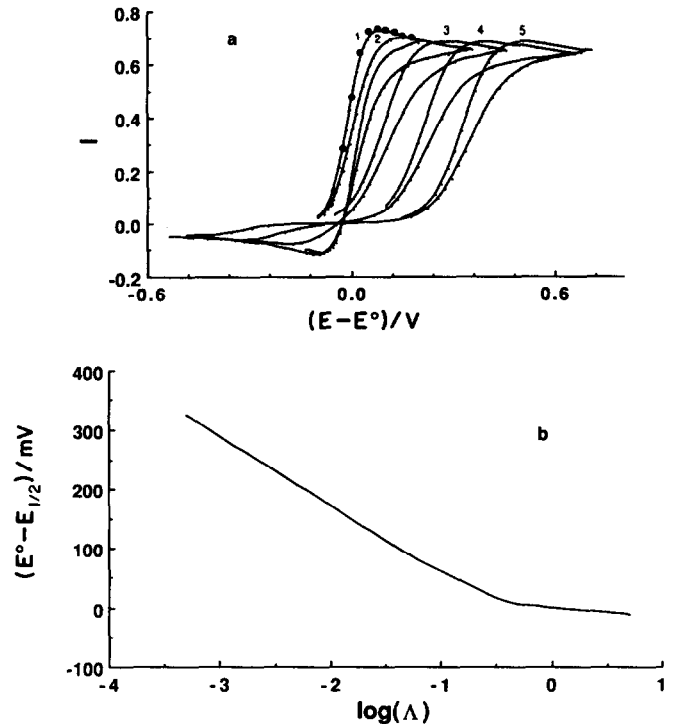

Fig. 4. Dimensionless CV at microband electrode approaching steady-state behavior: $\nu = fnvw^2/4D = 0.01$; $\alpha = 0.5$. Curve 1, $\Lambda = 5$; curve 2, $\Lambda = 0.5$; curve 3, $\Lambda = 0.05$; curve 4, $\Lambda = 5 \times 10^{-3}$; curve 5, $\Lambda = 5 \times 10^{-4}$ ($\Lambda = wk_s/2D$). Circles are from ref. 11 and are computed for a Nernstian charge transfer.

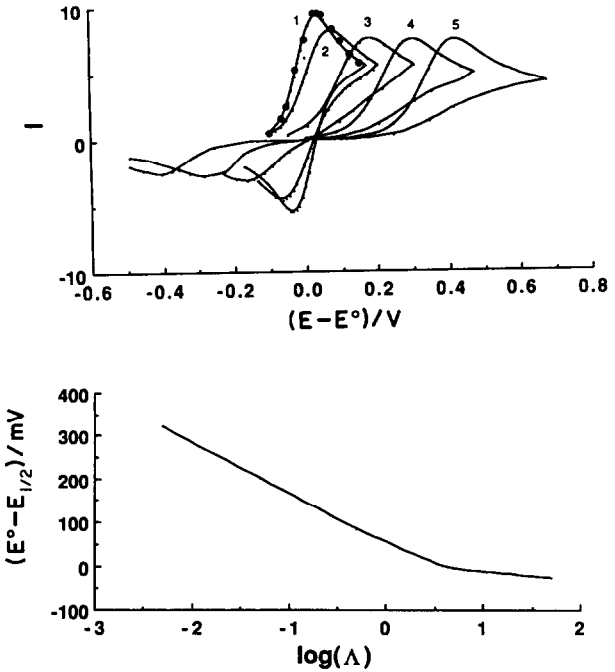

Fig. 5. Non-steady-state dimensionless CV at a microband electrode; $\nu = 100$; $\alpha = 0.5$. Curve 1, $\Lambda = 50$; curve 2, $\Lambda = 5$; curve 3, $\Lambda = 0.5$; curve 4, $\Lambda = 0.05$; curve 5, $\Lambda = 5 \times 10^{-3}$. Circles are from ref. 11 and are computed for a Nernstian charge transfer.

the shape of the CV is determined completely by the values of two kinetic parameters Λ and α, and the dimensionless scan rate $\nu = fnvw^2/4D$. The magnitude of ν, analogous to the "band factor" in ref. 10 determines whether the CV approaches steady-state (Fig. 4) or non-steady-state (Fig. 5) behavior. Curves 3–5 in both figures approach irreversibility, and their peak heights are virtually independent of Λ. Note that both quasi-steady-state and non-steady-state irreversible CVs show a ca. 118 mV shift of the half-peak potential with each order-of-magnitude change of Λ (Figs. 4(b) and 5(b)). This shift corresponds to $RT/\alpha nF$ at $T = 25°C$ and $\alpha = 0.5$, as found previously for the CV at a planar electrode [25] and for the steady-state CV at microsphere and microdisk electrodes [26]. The curves computed with $\Lambda = 5$, $\nu = 0.01$ (Fig. 4(a)) and $\Lambda = 50$, $\nu = 100$ (Fig. 5(a)) are vitually Nernstian. These curves can be compared with those computed in refs. 10 and 11. The extraction of the quantitative information from the small CVs given in ref. 10 was difficult; thus we compare our data with the reversible linear sweep voltammograms simulated in ref. 11. Figures 4(a) and 5(a) show excellent agreement for both the quasi-steady-state and non-steady-state voltammograms in ref. 11.

We also applied this approach to the examination of the interesting experimental results obtained with very small microband electrodes [3]. Small microband

widths, as discussed above, are particularly useful in studying rapid heterogeneous kinetics, and are easily fabricated by the film-deposition technique [3,13]. However, it was suggested that CVs obtained with very small band electrodes, i.e. those whose widths approach molecular dimensions, cannot be explained without taking into account the finite size of the electroactive particles because substantial deviations of the experimental curves from those predicted by conventional theory were seen [3]. Such a deviation would complicate the use of very small electrodes (including microdisks [27]) in studying rapid reactions. However, the conclusions of ref. 3 are based on approximate calculations of the expected limiting current using an equation for cylindrical diffusion and assuming zero surface concentration. Computations according to eqns. (1) and (2) show that the limiting dimensionless current for ferrocyanide oxidation under the conditions described in ref. 3, with $k_s = 0.1$ cm s^{-1} and $\alpha = 0.5$, should be $I = 0.333$ for a 500 Å wide band and $I = 0.280$ for a 100 Å wide band electrode. The experimental results shown in Fig. 2 of ref. 3 are about 0.33 and 0.0088. Thus the deviation of the experimental results for a 100 Å wide band is even larger than that found in the approximate treatment [3], i.e. the experimental value is 30 times smaller than expected (rather than 5–8 times smaller). Although this might be attributed to new considerations that become important when the band dimensions become very small, one must also consider the possibility that bands fabricated to these dimensions may deviate significantly from the ideally shaped bands assumed in the theoretical computations.

Double-band electrodes

There have been several previous theoretical treatments of double-band electrodes [12,13,15]. These have usually dealt with the arrangement where one electrode behaves as a generator and produces a product that is detected by the second (collector) electrode. In addition to this generator–collector (G–C) mode, one can also consider a shielding experiment where the flux of reactant to an electrode is intercepted by one or more adjacent electrodes [13]. For example, the generator and collector currents have been calculated for the G–C mode under the assumption of attainment of steady-state currents [12]. However, as discussed above, a true steady state is not achieved for the case of a band geometry, although a quasi-steady state should be attained. Several time-independent G–C curves which do not indicate the time range corresponding to this near-steady-state behavior were given in ref. 12. Computation, via digital simulations, of the complete current–time transients was described in ref. 13. Although our model allows consideration of a quite general situation (quasi-reversible charge transfer with different sets of kinetic parameters for generator and collector electrodes, arbitrary shapes of applied signals, non-uniform distribution of surface concentrations), we present here only the data comparable with the diffusion-controlled G–C mode results [12].

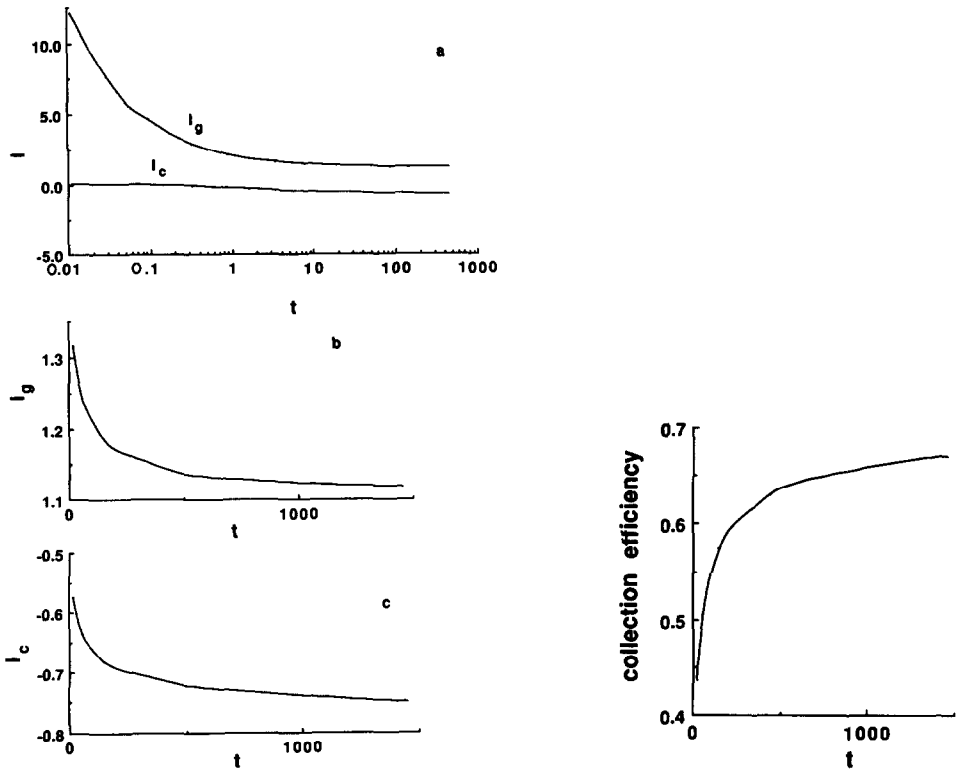

Fig. 6. Generator and collector transients computed for (a) a wide range of times and (b), (c) corresponding long-time curves: $\Lambda = 5$, $\alpha = 0.5$, $fn(E_g - E^\circ) = -5.87$, $fn(E_c - E^\circ) = 5.87$ and $g = 0.5$. I_c, I_g and t are defined as in Fig. 2.

Fig. 7. The collection efficiency I_c / I_g as a function of normalized time. See Fig. 6 for parameter values.

The generator and collector current transients shown in Fig. 6 are computed for $\Lambda = 5$, $fn(E_g - E^\circ) = -5.85$ and $fn(E_c - E^\circ) = 5.85$, values which assure that the process is apparently controlled by diffusion (Fig. 3). Even though the wide time range transients at closely spaced generator and collector electrodes ($g = 0.5$) virtually approach steady state (Fig. 6(a)), a more detailed consideration of the long-time region (Figs. 6(b) and 6(c)) shows that no actual steady state is achieved at $t = 1500$ (for the case of $D = 10^{-5}$ cm^2 s^{-1} and $w = 10$ μm, this value is about 40 s). The collection efficiency is also a function of time (Fig. 7), and it reaches the limiting value of about 0.69 at $t > 2000$. However, the working curve plotted in coordinates I_b/I_g versus I_c/I_g (I_b is a single-band current under the same conditions and at the same time) was virtually the same for any $t \geq 100$ (Fig. 8). In conclusion, the steady-state approximation [12] should be precise for small closely spaced microbands, i.e. $w \leq 1$–10 μm and $g \leq 1$—2. For larger electrodes and

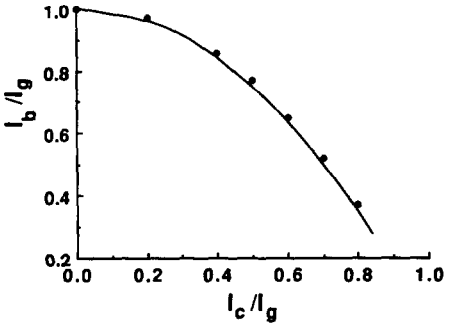

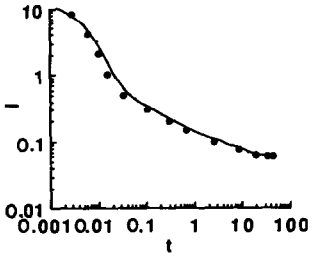

Fig. 8. Dimensionless working curve for the double-band electrode. The solid curve represents our results computed for g values from 0.01 to 1000 at $t = 1456.1$; for other parameters see Fig. 6. Circles correspond to the theoretical curve plotted in Fig. 5 of ref. 12.

Fig. 9. Dimensionless transient computed for SECM with an infinite insulated substrate and inlaid tip: $\gamma = 0.1$; for other parameters see Fig. 2. Circles are from ref. 18 and are computed assuming total diffusion control (zero surface concentration) at the tip and RG = 10.

spacings the collection efficiency may be significantly time dependent (in the absence of convective effects which become important at longer times).

Scanning electrochemical microscopy

As one can see from eqns. (9) and (10), a relatively wide set of parameters is needed to characterize the SECM experiment. In addition to the tip radius and tip–substrate distance, which are the key parameters for diffusion-controlled processes [16,17], in the general case one must also specify heterogeneous kinetic parameters for tip and substrate. Moreover, the relative size of the substrate can be a factor, unless it is significantly larger than the tip. In this paper we consider the tip current transient above an infinite insulator and show that it agrees with that calculated using the Krylov integrator [17] and the ADI method [18]. We then consider the SECM CV above a conductive substrate of a size equal to the tip and the effect of a homogeneous reaction of the tip-generated product in the gap region.

SECM with an insulating substrate

This type of experiment is important for surface imaging. The rate of charge transfer is not of great interest, but the problem to be solved here is the significance of the influence of the insulating sheath geometry on the tip transient and especially the near-steady-state current. For SECM with an insulating substrate this factor is expected to be much more significant than that in the case of conductive substrate [16]. At the same time, it is quite difficult to construct the rigorous theory for a non-inlaid tip SECM, even in the case of perfect cylindrical

geometry of the insulating sheath [1]. The real SECM tip is usually sealed into a conical—rather than cylindrical—glass sheath. The theory for such a geometry is unavailable.

The treatment in ref. 16 describes only the steady-state situation. No estimate was made for the time required for this steady state to be achieved. Obviously, the influence of the finite insulator radius will be observed only at the time when the thickness of the diffusion layer (approximately equal to $(DT)^{1/2}$) becomes comparable with this radius. This condition can be written in the dimensionless form

$$\left(DR_t^2 t/D\right)^{1/2} > \mathrm{RG}R_t \quad \text{or } t > \mathrm{RG}^2 \tag{20}$$

For RG = 10, 100 and 1000 [16], the corresponding t values from eqn. (20) are 10^2, 10^4 and 10^6. Assuming $R_t = 5$ μm and $D = 10^{-5}$ cm^2 s^{-1}, these values correspond to 2.5 s, 250 s and 2.5×10^4 s. The last two values are impractical in actual experiments and even the first is somewhat high for an imaging time-scale. For a rate of tip scanning over the substrate surface of 10 μm s^{-1}, the tip displacement during 2.5 s is 25 μm, i.e. quite a large value compared with $R_t = 5$ μm. The conclusion is that the steady-state current recorded during the surface observation should be essentially independent of RG, when RG $\geq$ 10.

The validity of this picture can be confirmed by comparison of the transient calculated from eqn. (9), assuming an infinite insulating substrate ($f_s = 0$) and inlaid tip, with that computed in ref. 18 for RG = 10 (Fig. 9). Despite minor discrepancies observed in a short-time region, both curves show the same value of steady-state current $I_{ss} = 0.059$ which is also in good agreement with the value given in ref. 16 for RG = 10. This apparent steady state has been achieved at $t \approx 30$–40, which is significantly smaller than the $t = 100$ which holds when the influence of a finite value RG = 10 becomes noticeable. If we continued the calculation of the current using eqn. (9), it would decrease very slowly and should reach the values predicted in ref. 16 for RG = 100 and RG = 1000 at the corresponding times. However, to describe a quasi-steady-state response observed in a real SECM experiment, computation of the current to reasonable times corresponding to the experimental time-scale needs be carried out. Thus, in practice, the SECM current is largely unaffected by RG. Notice that an apparent steady state is observed at $t < 100$ with any values of R_t, γ and RG. While the computation of the transient (Fig. 9) using the ADI method required thousands of time iterations, the transient computed by the approach described here used 41 t-points.

SECM with a conductive substrate

Although CVs at an SECM tip in close proximity to a conductive substrate were obtained experimentally [20], no theory is available under either steady-state or non-steady-state conditions. Similarly, no theoretical treatment is available for SECM with heterogeneous kinetic effects on the substrate; experimental results with the Fe^{3+}–Fe^{2+} system at a glassy carbon substrate have appeared [22]. The dependence of the CV shape on the kinetic parameter Λ, as well as the effect of

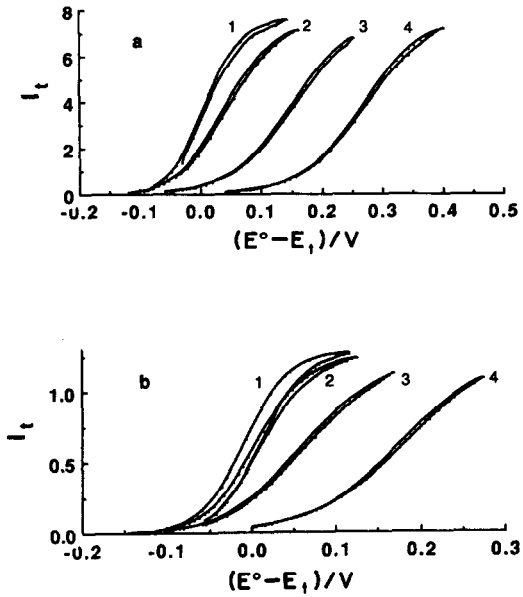

Fig. 10. Steady-state tip CV in SECM as a function of the mediator oxidation–reduction rate and the γ value: $\nu = fnvR_t^2/D = 0.01$, $\alpha = 0.5$, $fn(E_s - E°) = 5.87$, $\Lambda_s = 5$. $\gamma = d/R_t$ has values of (a) 0.1 and (b) 1. Curve 1, $\Lambda_t = 25$; curve 2, $\Lambda = 5$; curve 3, $\Lambda = 0.5$; curve 4, $\Lambda = 0.05$.

the tip–substrate spacing d are shown in Figs. 10 and 11. The sequence of the near-steady-state tip CV computed with the different values of Λ_t (Fig. 10) are similar to those computed previously for a microdisk electrode [1]. However, as proposed earlier [22], at a small value of γ (Fig. 10(a)) the half-wave potential is more sensitive to the charge transfer rate than is $E_{1/2}$ of the microdisk CVs (with the same disk radius) at large d. When γ increases (Fig. 10(b)), the feedback current drops dramatically and the CVs become more closely spaced. Thus in studies of heterogeneous kinetic effects at a microdisk [28], the relevant dimensionless parameter changes from $k_s R_0/D$ to $k_s d/D$ as a conductive substrate is approached by the disk. This suggests that the SECM should be useful for studying rapid heterogeneous electron transfer kinetics, since it should be easier to obtain very small (and variable) tip–substrate spacings than to produce microdisks with equally small radii.

If the tip and the substrate radii are of the same order of magnitude and they are in close proximity, the current flowing at one electrode can be affected by changing the potential of the other. For example, a linear sweep of the tip potential in a negative direction (the forward portion of Fig. 10(a), curve 2) produces an anodic current at the substrate, when its potential is constant and held where the tip-generated product is oxidized at the substrate (Fig. 11(a)). In this case, the tip behaves as a generator and the substrate behaves as a collector electrode. Note that the collection efficiency is near unity, even for a small

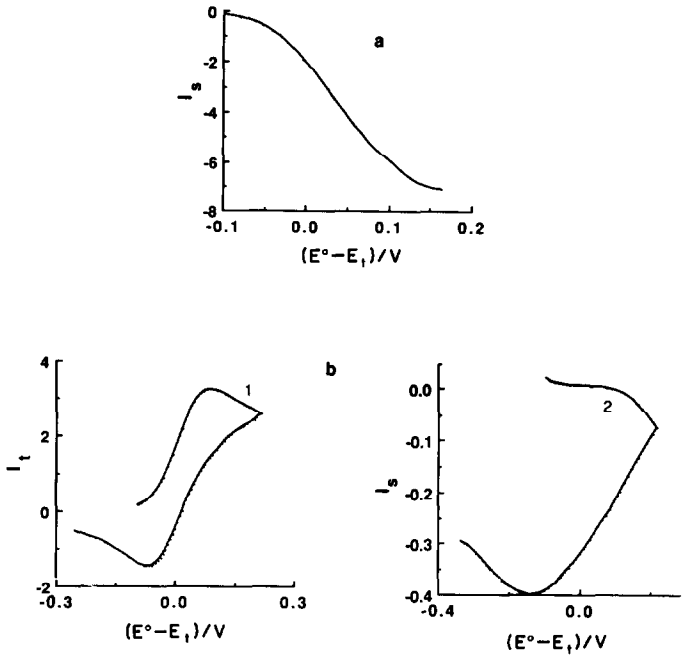

Fig. 11. Voltammogram-like curves produced at a constant potential-biased substrate by a linear sweep of the tip potential ($fn(E_s - E°) = 5.87$): (a) substrate response corresponding to the forward portion of the steady-state tip CV (Fig. 10(a), curve 2); (b) non-steady-state tip CV (curve 1) and the substrate response (curve 2) at a higher scan rate ($\nu = 100$). For other parameters see Fig. 10(b), curve 2.

substrate ($R_s = R_t$) at this value of γ. The symmetry of the problem implies that identical results will be obtained in a G–C experiment when the tip is the collector. One can expect some delay in the substrate response to the change of the tip potential, because it depends on the γ, D and υ values. This delay is not seen in Fig. 11(a) because of the small values of γ and υ. When the sweep is fast (or γ is not as small) (Fig. 11(b)), the delay between the cathodic peak of the tip voltammogram (curve 1) and the substrate anodic peak is substantial. Pairs of such curves should contain information about the diffusional and electrochemical kinetics of the redox couple in the gap.

SECM appears to be promising in obtaining selective images of materials composed of different components [23]. These components can be distinguished by the difference in the rate constant of the mediator oxidation–reduction at their surfaces. Figure 12 allows the effect of Λ_s on the steady-state tip current to be estimated. The observed tip current can be understood in terms of two opposite tendencies. The blocking effect of the substrate tends to decrease I_t when Λ_s is small (tending to ideal insulator behavior at $\Lambda_s = 0$), and the positive feedback effect tends to increase I_t when Λ_s is large and γ is small. Several conclusions can be drawn from Fig. 12.

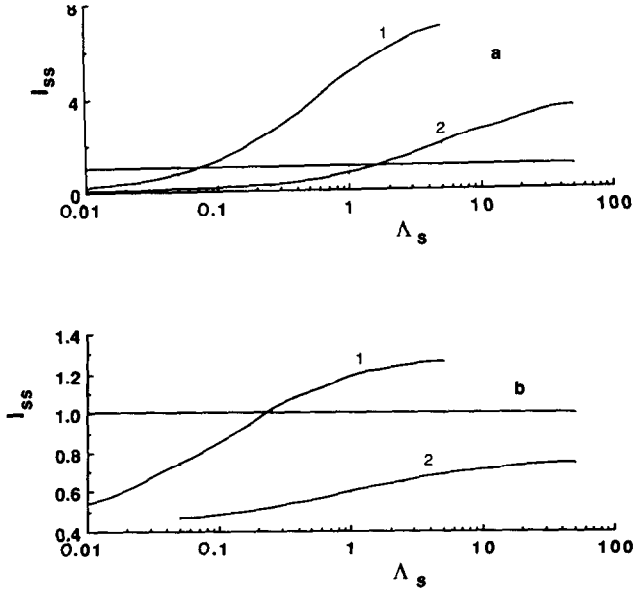

Fig. 12. Dependence of the steady-state tip current on Λ_s. $\alpha = 0.5$, $fn(E_t - E^\circ) = -5.87$ with (a) $\gamma = 0.1$ and (b) $\gamma = 1$: curve 1, $fn(E_s - E^\circ) = 5.87$; curve 2, $fn(E_s - E^\circ) = 0$. The horizontal line corresponds to zero feedback current. $\Lambda_s = R_t k_{s,s}/D$.

(i) When the tip is sufficiently close to the substrate (Fig. 12(a)), one can distinguish between the substrate components with a ratio of rate constants as low as 2:1.

(ii) By choosing the proper E_s value, one can image the more electroactive part of the substrate as a conductor ($I_{ss} > 1$ and $dI_{ss}/d\gamma < 0$) and the less active part as an insulator ($I_{ss} < 1$ and $dI_{ss}/d\gamma > 0$), as was shown experimentally in ref. 23.

(iii) Comparing curves 1 in Figs. 12(a) and 12(b), and curves 2 in Figs. 12(a) and 12(b), one can see that a substrate with the same values of Λ_s and E_s may behave as a conductive substrate when it is close to the tip, and as an insulating substrate at larger γ. Clearly the conductive (positive feedback) or insulating (blocking) effect of the substrate is determined only by the average value of the mediator concentration $c_{Ox}(t, \gamma)$ generated by the substrate at a distance γ from the tip surface. If this value is greater than $c^{\infty}_{Ox}(t, \gamma)$ (the concentration value at the same distance from the tip which would exist if the substrate were removed), a conductive substrate is observed. If $c_{Ox}(t, \gamma) < c^{\infty}_{Ox}(t, \gamma)$, the substrate looks more like an insulator. Since $c^{\infty}_{Ox}(t, \gamma)$ increases with γ, the same substrate may appear as a conductor when γ is small, and as an insulator at larger γ values. This effect should be observed experimentally when E_s is not very high.

(iv) The steady-state current computed with a small γ and an E_s value close to E° is the most sensitive to Λ_s. There is a significant difference (about 10%) between I_{ss} values corresponding to $\Lambda_s = 25$ and $\Lambda_s = 50$. These measurements

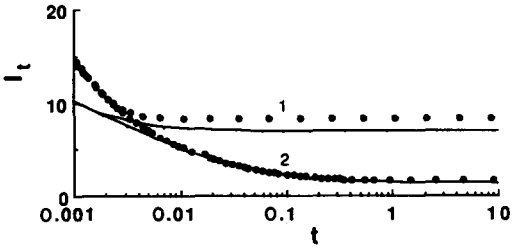

Fig. 13. The tip current computed for SECM with a conductive substrate of the same size as the tip: $E_s = -E_t$, $\Lambda_t = 5$; other parameters are the same for both the tip and the substrate (see Fig. 12) Curve 1, $\gamma = 0.1$; curve 2, $\gamma = 1$. Circles are from ref. 18 and are computed for an infinite conductive substrate and total diffusion control (very large k_s).

may be useful in the determination of kinetic parameters for very fast reactions. The ratio of the tip to the substrate steady-state currents (if the latter is also a microdisk) is quite sensitive to the Λ_s value.

In the case of a conductive substrate the effect of the geometry of the insulator surrounding the tip (RG) is unimportant [16] because the steady state is achieved in a very short time and the steady-state current is quite high. The influence of the substrate size is more interesting, because it can lead to erroneous interpretations of the image when the observed surface includes small areas (of the order of R_t) composed of different materials. As expected, the positive feedback tip current is about 20% higher in the case of an infinite conductive substrate compared with one of finite size ($R_t = R_s$), and either $\gamma = 0.1$ or $\gamma = 1$ (Fig. 13). If the rates of the electrochemical reaction at different parts of the substrate are of the same order of magnitude, this effect can also be quite substantial.

Incorporation of homogeneous chemistry in the gap

Many first-order homogeneous chemical reactions coupled with charge transfer can be incorporated into microelectrode theory using an approach similar to that proposed in ref. 29 for semi-infinite linear diffusion. A general discussion of this topic is beyond the scope of this article, and we present here only the example of SECM equations for E_qC_i (quasi-reversible charge transfer followed by the irreversible first-order chemical reaction) (see also ref. 18). The dimensionless diffusion problem for this case is as follows:

$$\frac{\partial c_{Ox}}{\partial t} = \frac{\partial^2 c_{Ox}}{\partial z^2} + \frac{\partial^2 c_{Ox}}{\partial r^2} + \frac{1}{r}\frac{\partial c_{Ox}}{\partial r} \qquad 0 < t,\ 0 \le r,\ 0 < z < \gamma \tag{21}$$

$$\frac{\partial c_{Red}}{\partial t} = \frac{\partial^2 c_{Red}}{\partial z^2} + \frac{\partial^2 c_{Red}}{\partial r^2} + \frac{1}{r}\frac{\partial c_{Red}}{\partial r} - \frac{R_t^2}{D}k \qquad 0 < t,\ 0 \le r,\ 0 < z < \gamma \tag{22}$$

$$t = 0,\ 0 \le r,\ 0 < z < \gamma \qquad c_{Ox}(0, r, z) = 0 \qquad c_{Red}(0, r, z) = 0 \tag{23}$$

$$0 < t,\ 0 \le r < 1,\ z = 0;$$

$$f_t(t, r) = -\Lambda_t\{[1 - c_{Ox}(t, r, 0)]\ \exp\{-\alpha_t f_t n[E_t(t) - E^\circ]\}$$
$$- c_{Red}(t, r, 0)\ \exp\{(1-\alpha_t) f_t n[E_t(t) - E^\circ]\}\};\quad 1 < r,\ f_t(t, r) = 0 \tag{24}$$

$$0 < t,\ 0 \le r < h,\ z = \gamma;$$

$$f_s(t, r) = -\Lambda_s\{[1 - c_{Ox}(t, r, \gamma)]\ \exp\{-\alpha_s f_s n[E_s(t) - E^\circ]\}$$
$$- c_{Red}(t, r, \gamma)\ \exp\{(1-\alpha_s) f_s n[E_s(t) - E^\circ]\}\};\quad h < r,\ f_s(t, r) = 0 \tag{25}$$

Equation (21) was solved in ref. 1, and the expressions for $c_{Ox}(t, r)$ at the tip and substrate surfaces were obtained; thus only the solution of eqn. (22) is of interest here. Applying Laplace and Hanckel transformations to eqn. (22) taking into account eqn. (23), as in ref. 1, yields

$$\frac{d^2\bar{\bar{c}}(s, p, z)}{dz^2} - (p^2 + k_1 + s)\bar{\bar{c}}(s, p, z) = 0 \tag{26}$$

where $k_1 = kR_t^2/D$. The only difference between eqn. (26) and eqn. (15) in ref. 1 is the presence of the additional constant k_1 associated with the chemical reaction. The method of solving eqn. (26) is completely identical to that described in ref. 1 and leads to the following expressions for surface concentrations:

$$c_{Red}(t, r, 0)$$
$$= -\frac{1}{2\gamma}\int_0^h u\,du \int_0^t \frac{\exp[-(r^2+u^2)/4(t-\tau) - k_1(t-\tau)]}{t-\tau}$$
$$\times I_o\left[\frac{ru}{2(t-\tau)}\right]\left\{f_s(\tau, u)\theta_4\left[0\middle|\frac{i\pi(t-\tau)}{\gamma^2}\right] + f_t(\tau, u)\theta_3\left[0\middle|\frac{i\pi(t-\tau)}{\gamma^2}\right]\right\} d\tau \tag{27}$$

$$c_{Red}(t, r, \gamma)$$
$$= -\frac{1}{2\gamma}\int_0^h u\,du \int_0^t \frac{\exp[-(r^2+u^2)/4(t-\tau) - k_1(t-\tau)]}{t-\tau}$$
$$\times I_0\left[\frac{ru}{2(t-\tau)}\right]\left\{f_s(\tau, u)\theta_3\left[0\middle|\frac{i\pi(t-\tau)}{\gamma^2}\right] + f_t(\tau, u)\theta_4\left[0\middle|\frac{i\pi(t-\tau)}{\gamma^2}\right]\right\} d\tau \tag{28}$$

Combination of eqns. (27) and (28) with eqns. (42) and (43) from ref. 1 (for the surface concentrations of the oxidized form) and the Butler–Volmer eqns. (24) and (25) yields the solution of the E_qC_i problem for the SECM. Analogous solutions can be derived for the other microelectrode geometries considered in ref. 1.

CONCLUSIONS

This study has demonstrated that the theory for a wide class of microelectrodes can be addressed using the multidimensional integral equation approach, and only minor changes are required to switch from one type of geometry to another or to incorporate first-order homogeneous reactions. The computational efficiency of this method is very high. The accuracy of the results is virtually independent of the spatial grid features. Most of the data necessary for comparison with experiments can be computed and presented in the form of dimensionless working curves. Currently, computer programs are under development that involve more versatile temporal grids.

ACKNOWLEDGMENTS

The support of this research by SACHEM and the National Science Foundation (CHE 8901450) is gratefully acknowledged. Our thanks are due to Dr. P. Unwin for providing transient SECM data for comparison and to Dr. D.O. Wipf for helpful discussions. The computing resources for this work were provided by The University of Texas System Center for High Performance Computing.

NOMENCLATURE

a_{j-1}, a_j	boundaries of the jth integration subinterval over the electrode surface
a_{lj}	elements of the matrix **A** in eqn. (3)
$\boldsymbol{b}$, b_l	column vector on the right-hand side of eqn. (3) and its elements
$c(t, r, z)$	dimensionless surface concentrations of the electroactive species as functions of spatial variables and time. The subscript Ox relates to the oxidized form and the reduced form
c°	bulk concentration
d	distance between tip and substrate electrodes in SECM
$E_{1/2}$	half-wave potential
$E(t)$	instantaneous value of the electrode potential; the subscripts t, s, g and c relate to the tip, the substrate, the generator and the collector electrode respectively
g	ratio of the gap width to the band width for a double-band electrode
h	ratio of the substrate radius to the tip radius
$I(T)$, $I(t)$	faradaic current and the same variable in dimensionless form
I_g, I_c	dimensionless generator and collector currents
I_{ss}	dimensionless steady-state current
I_0	modified Bessel function of the first kind of order zero
k	first-order homogeneous rate constant
L	microband length

R_t, R_s	tip and substrate radii in SECM
R, r	radial distance from the tip center and the same variable in the dimensionless form; $r = R/R_t$
RG	ratio of the radius of the glass sheath surrounding the tip to R_t
T, t	time and its dimensionless value equal to DT/R_t^2 for the SECM and $4DT/w^2$ for a microband electrode
υ, ν	scan rate and the same parameter in the dimensionless form
w	microband width
X, x	normal distance from the band electrode surface and the same variable in the dimensionless form: $x = 2X/w$
γ	$= d/R_t$ dimensionless distance between two electrodes in the SECM
Λ, Λ_t, Λ_s	dimensionless kinetic parameters, equal to $wk_s/2D$, $R_t k_{s,t}/D$ and $R_t k_{s,s}/D$ for a microband, SECM tip and substrate respectively
$\theta_i(0 \mid \gamma)$	θ functions, $i = 1, 2, 3, 4$

Other symbols are defined in Part 1 [1].

REFERENCES

1 M.V. Mirkin and A.J. Bard, J. Electroanal. Chem., 323 (1992) 1–27.
2 K.R. Wehmeyer, M.R. Deakin and R.M. Wightman, Anal. Chem., 1913 (1985) 57.
3 R.B. Morris, D.J. Franta and H.S. White, J. Phys. Chem., 91 (1987) 3559.
4 W. Thormann, P. van den Bosch and A.M. Bond, Anal. Chem., 57 (1985) 2764.
5 A.M. Bond, T.L.E. Henderson and W. Thormann, J. Phys. Chem., 90 (1986) 2911.
6 P.M. Kovach, W.L Caudill, D.G. Peters and R.M. Wightman, J. Electroanal. Chem., 185 (1985) 285.
7 K. Aoki, K. Tokuda and H. Matsuda, J. Electroanal. Chem., 225 (1987) 19.
8 A. Szabo, D.K. Cope, D.E. Tallman, P.M. Kovach and R.M. Wightman, J. Electroanal. Chem., 217 (1987) 417.
9 S. Coen, D.K. Cope and D.E. Tallman, J. Electroanal. Chem., 215 (1986) 29.
10 M.R. Deakin, R.M. Wightman and C.A. Amatore, J. Electroanal. Chem., 215 (1986) 49.
11 C.A. Amatore, B. Fosset, M.R. Deakin and R.M. Wightman, J. Electroanal. Chem., 225 (1987) 33.
12 B. Fosset, C.A. Amatore, J.E. Bartelt, A.C. Michael and R.M. Wightman, Anal. Chem., 63 (1991) 306, and references cited therein.
13 T. Varco Shea and A.J. Bard, Anal. Chem., 59 (1987) 2101.
14 L.E. Fosdick, J.L. Anderson, T.A. Baginski and R.C. Jaeger, Anal. Chem., 58 (1986) 2750, and references cited therein.
15 S. Licht, V. Cammarata and M.S. Wrighton, J. Phys. Chem., 94 (1990) 6133.
16 J. Kwak and A.J. Bard, Anal. Chem., 61 (1989) 1221.
17 A.J. Bard, G. Denuault, B.C. Dornblaser, R.A. Friesner and L.S. Tuckerman, Anal. Chem., 63 (1991) 1282.
18 P.R. Unwin and A.J. Bard, J. Phys. Chem., 95 (1991) 7814.
19 G. Denuault, Ph.D. Thesis, University of Southampton, 1989.
20 A.J. Bard, F.-R.F. Fan, J. Kwak and O. Lev, Anal. Chem., 61 (1989) 132.
21 A.J. Bard, G. Denuault, C. Lee, D. Mandler and D.O. Wipf, Acc. Chem. Res., 23 (1990) 357, and references cited therein.
22 D.O. Wipf and A.J. Bard, J. Electrochem. Soc., 138 (1991) 469.

23 D.O. Wipf and A.J. Bard, J. Electrochem. Soc., 138 (1991) L4.
24 H. Bateman, Tables of Integral Transforms, Vol. 1, McGraw-Hill, New York, 1954, p. 388.
25 R.S. Nicholson and I. Shain, Anal. Chem., 36 (1964) 706.
26 A.M. Bond, K.B. Oldham and C.G. Zoski, J. Electroanal. Chem., 245 (1988) 71.
27 R.M. Penner, M.J. Heben, T.L. Longin and N.S. Lewis, Science, 250 (1990) 1118.
28 K.B. Oldham, J.C. Myland, C.G. Zoski and A.M. Bond, J. Electroanal. Chem., 270 (1989) 79.
29 M.V. Mirkin, A.P. Nilov and M.K. Nauryzbaev, J. Electroanal. Chem., 281 (1990) 41.